THE ASTROPHYSICAL JOURNAL, 998:75 (15pp), 2026 February 10 https://doi.org/10.3847/1538-4357/ae2d56

3D MHD Simulations of Coronal Loops Heated via Magnetic Braiding. I. Continuous Driving

G. Cozzo[1,2], Paola Testa[1], J. Martinez-Sykora[3,4,5,6], F. Reale[2,7], P. Pagano[2,7], F. Rappazzo[2,7], V. Hansteen[4,5,6], B. De Pontieu[4,5,8], A. Petralia[2], E. Alaimo[2,7], F. Fiorentino[2,7], F. D'Anca[2], L. Sciortino[2,7], M. Todaro[2], U. Lo Cicero[2], and M. Barbera[2,7]

[1] Harvard—Smithsonian Center for Astrophysics, 60 Garden St., Cambridge, MA 02193, USA; gabriele.cozzo@cfa@harvard.edu
[2] INAF—Osservatorio Astronomico di Palermo, Piazza del Parlamento 1, I-90134 Palermo, Italy
[3] Lockheed Martin Solar and Astrophysics Laboratory, 3251 Hanover St, Palo Alto, CA 94304, USA
[4] Rosseland Centre for Solar Physics, University of Oslo, P.O. Box 1029 Blindern, N-0315 Oslo, Norway
[5] Institute of Theoretical Astrophysics, University of Oslo, P.O. Box 1029 Blindern, N-0315 Oslo, Norway
[6] SETI Institute, 339 Bernardo Ave, Suite 200, Mountain View, CA 94043, USA
[7] Dipartimento di Fisica & Chimica, Università di Palermo, Via Archirafi 36, 90123 Palermo, Italy
[8] Lockheed Martin Solar & Astrophysics Laboratory, 3251 Hanover St., Palo Alto, CA 94304, USA
Received 2025 September 28; revised 2025 December 8; accepted 2025 December 14; published 2026 February 4

Abstract

The nature and detailed properties of the heating of the million-degree solar corona are important issues that are still largely unresolved. Nanoflare heating might be dominant in active regions and quiet Sun, although direct signatures of such small-scale events are difficult to observe in the highly conducting, faint corona. The aim of this work is to test the theory of coronal heating by nanoflares in braided magnetic field structures. We analyze a 3D MHD model of a multistrand flux tube in a stratified solar atmosphere, driven by twisting motions at the boundaries. We show how the magnetic structure is maintained at high temperature and for an indefinite time, by intermittent episodes of local magnetic energy release due to reconnection. We synthesize the optically thin emission with SDO/AIA and MUSE and compare the synthetic observations with the intrinsic coronal plasma properties, focusing on the response to impulsive coronal heating. Currents' buildup and their impulsive dissipation into heat are also investigated through different runs. In this first paper, we describe the proliferation of heating from the dissipation of narrow current sheets in realistic simulations of braided coronal flux tubes at unprecedented high spatial resolutions.

Unified Astronomy Thesaurus concepts: Space plasmas (1544); Solar physics (1476); Solar corona (1483); Magnetohydrodynamical simulations (1966); Solar magnetic reconnection (1504); Solar coronal loops (1485)

Materials only available in the online version of record: animations

1. Introduction

The million-degree solar corona owes its extreme temperature to the continuous driving of energy from the coronal magnetic field to its tenuous plasma (H. Alfvén 1947; E. N. Parker 1988; J. A. Klimchuk 2015; P. Testa et al. 2015; P. Testa & F. Reale 2023). In extreme ultraviolet (EUV) and X-ray images, this interaction manifests itself as bundles of bright, arch-shaped strands, the coronal loops, that outline closed magnetic flux tubes linking opposite-polarity regions in the photosphere (G. Vaiana et al. 1973; F. Reale 2014). Identifying the physical processes that maintain such hot structures remains one of the central challenges of solar physics (W. Grotrian 1939; B. Edlén 1943; H. Peter & B. N. Dwivedi 2014).

Coronal loops remain bright for hours, much longer than their characteristic cooling times (R. Rosner et al. 1978). For most of their lifetime, they can therefore be described as systems in equilibrium (M. Landini & B. Monsignori Fossi 1975). The rise, steady, and decay phases of their emission imply that the average heating rate slowly grows, plateaus, and declines. Observations revealed that coronal loops are also highly dynamic and structured, both spatially and thermally. Fuzziness seen in harder X-ray bands and hotter spectral lines has been interpreted as evidence that each loop is a bundle of thin, unresolved strands heated in pulses (M. Guarrasi et al. 2010). To explain both the long-lived brightness and the fine structure, several authors have argued that loops are not in true equilibrium. Instead, they are filamented and continuously cool from a hotter state while undergoing repeated heating episodes (P. J. Cargill & J. A. Klimchuk 2004).

In the classic picture proposed by E. N. Parker (1988), random footpoint shuffling braids coronal field lines into ever more tangled configurations. At sufficiently small spatial scales (strands of the order of 10–100 km wide, according to both observations and models; C. Beveridge et al. 2003; J. Klimchuk et al. 2008; G. Vekstein 2009), intense current sheets must form. Reconnection across those sheets releases packets of magnetic energy of order 10^{24} erg, the so-called "nanoflares" (E. N. Parker 1988), believed to be the small-energy limit of a "syndrome" (H. Hudson 2010) of observed phenomena with energies following a frequency power-law of index $\sim$−1.8. (J. F. Drake 1971; B. R. Dennis 1985; N. B. Crosby et al. 1993). Individual nanoflares are often difficult to isolate observationally (e.g., P. Testa et al. 2013, 2014, 2020; K. Cho et al. 2023), as thermal conduction rapidly spreads the heat along the reconnected field lines (e.g., B. V. Gudiksen & Å. Nordlund 2005).

Ab initio and boundary-driven 3D MHD simulations offer complementary views of how energy is transported into and dissipated within coronal loops. Ab initio models that extend from the upper convection zone through the photosphere, chromosphere, and transition region self-consistently produce loop turbulence, current-sheet formation, and intermittent heating; e.g., C. Breu et al. (2022) model a straightened flux tube with MURaM (A. Vögler et al. 2005; M. Rempel 2016) and recover transient bright strands in synthesized AIA/XRT emission (L. Golub et al. 2007; J. R. Lemen et al. 2012). Boundary-driven studies similarly reveal that complex footpoint motions promote the proliferation and dissipation of thin current sheets and bursty energy release, with heating characteristics that depend on the frequency and amplitude of the driver (T. A. Howson & I. De Moortel 2022). Taken together, these simulations link together magnetic braiding, turbulence, and reconnection, establishing a consistent mesoscale picture of coronal loop structuring and heating.

The merging of two or more twisted flux ropes is also considered a potential mechanism for releasing stored magnetic energy, leading to both large-scale flares, and on smaller scales, to coronal heating by nanoflares (e.g., T. Gold & F. Hoyle 1960; D. Melrose 1997; D. Kondrashov et al. 1999). Reconnection and energy release during flux-rope mergers have been both modeled (e.g., M. Linton et al. 2001; B. Kliem et al. 2014) and observed in various eruptive events (R. Liu 2020). Recent 2.5D simulations by S. Sen & F. Moreno-Insertis (2025) using the MPI-AMRVAC code have revealed that the interaction and merging of flux ropes can also lead to nanojet-like ejections, similar to the reconnection outflows obtained from the merging of two misaligned magnetic flux tubes in P. Antolin et al. (2021) and G. Cozzo et al. (2025).

Lare3D (T. Arber et al. 2001) simulations show that in a multistrand, nonpotential coronal loop, a single kink-unstable thread can trigger an avalanche of reconnection across neighboring strands, even if they are individually subcritical (K. V. Tam et al. 2015; A. W. Hood et al. 2016). Once a strand exceeds the kink twist threshold, a helical current sheet forms, fragments, and dissipates, producing nanoflare-like bursts (H. Baty & J. Heyvaerts 1996; A. Hood et al. 2009). The resulting heating is intermittent, with short spikes rather than steady dissipation, providing a triggered mechanism for loop energization. Energy injected by photospheric motions is released via viscous and ohmic dissipation during relaxation, and under continuous driving, through repeated impulsive, localized events (J. Reid et al. 2018, 2020). Whether further avalanche onsets are suppressed by field disorder remains debated (A. Rappazzo et al. 2013). Following three neighboring threads twisted by a footpoint driver, J. Reid et al. (2018, 2020) confirmed that the destabilization of a single node can trigger the release of magnetic energy across all three and sustain bursty heating; with ongoing twisting, the corona approaches a statistically steady state in which intermittent pulses balance radiative and conductive losses.

PLUTO (A. Mignone et al. 2007) simulations described in G. Cozzo et al. (2023) extended previous MHD avalanche models, accounting for a fully stratified upper-atmosphere (chromosphere, transition region, and corona, modeled through Spitzer thermal conduction (L. Spitzer & R. Härm 1953), optically thin radiative losses, and gravity), allowing for detailed forward modeling of emission in optically thin EUV lines (G. Cozzo et al. 2024). Recently, C. D. Johnston et al. (2025) showed that twisting-induced MHD avalanches can lead to strong and compact events of energy release (nanoflare storms) that may be responsible for the bright loops that stand out in the corona against the diffuse EUV emission.

The forthcoming Multi-slit Solar Explorer (MUSE; B. De Pontieu et al. 2019) will address coronal loop heating through high-cadence, high-resolution EUV spectroscopy, delivering simultaneous constraints on brightness, Doppler shifts, and nonthermal line widths over a broad temperature range (MUSE; B. De Pontieu et al. 2022). This will provide new insights on how magnetic reconnection operates within coronal magnetic flux strands, the fundamental elements of loops and active regions, and will open new avenues for diagnosing coronal heating. In preparation, a more complete theoretical and numerical framework for DC heating via component 3D reconnection (M. Hesse & K. Schindler 1988; K. Schindler et al. 1988) in braided fields is required and must be tested in a realistic coronal environment that includes chromospheric and photospheric coupling layers that supply both Poynting flux and mass to the corona through nonlinear MHD processes (C. E. Parnell & I. De Moortel 2012).

For instance, building on the G. Cozzo et al. (2023) setup, G. Cozzo et al. (2024) sampled at the MUSE expected pixel scale, cadence, and temperature response. They found that MUSE could resolve fine structures from tube fragmentation, including footpoint evaporation upflows (Fe IX line at 171 Å), bulk loop brightening with alternating filamentary Doppler patterns (Fe XV line at 284 Å), and transient brightenings of folded sheet-like structures bounding unstable strands (Fe XIX line at 108 Å). In a following work, G. Cozzo et al. (2025) developed diagnostics for reconnection outflows in hot coronal loops, widely interpreted as signatures of ubiquitous small-angle component reconnection in the solar corona (P. Antolin et al. 2021). They showed that the MUSE spectrograph can isolate EUV lines selectively sensitive to hot plasma, offering clear advantages over previous instruments, due to its high-temperature sensitivity and its ability to detect the predicted bidirectional Doppler shifts. Overall, the predicted signatures indicate that MUSE can pinpoint key dynamics of ignition and reconnection, providing discriminating diagnostics of the underlying heating processes.

The next step is to address the long temporal brightening of observed coronal loops and the role of DC heating in coronal close magnetic flux tubes. With this aim, in this paper, we investigated the post-avalanche phase of the coronal flux tubes in a stratified solar atmosphere. Specifically, we pursued mesoscale simulations that track a few strands, trading domain extent for the resolution needed to capture current-sheet formation, thinning, and reconnection outflows, physics that is generally addressed only in simpler reduced-MHD or 2.5D studies (e.g., A. Rappazzo et al. 2013), while incorporating key coronal ingredients (e.g., anisotropic conduction and optically thin radiative losses) generally used in large-scale AR simulation, to enable observation-driven validation. A continuous footpoint driver (J. Reid et al. 2018) powers a nearly constant Poynting flux into the corona. We consider a timescale sufficiently long as to reach a steady state. We address the energy buildup of the already fragmented magnetic field and its intermittent, impulsive dissipation within narrow current sheets.

In Section 2, we describe the model. in Section 3, we report on the evolution of the coronal loop on a global scale, on the reconnection processes occurring in the post-avalanche phase of the loop evolution, on forward-modeling results of EUV emission in AIA channels and MUSE spectral lines (B. De Pontieu et al. 2022), and on the role of magnetic diffusivity, through the analysis of different runs with different numerical parameters. We draw our conclusions in Section 4.

2. Model

We used a model of a magnetized solar atmosphere in a 3D Cartesian box where interacting and twisted coronal loop strands are braided at subarcsec scales, similar to the work presented by G. Cozzo et al. (2023) and F. Reale et al. (2016).

The simulations are performed using the PLUTO code (A. Mignone et al. 2007), a modular Godunov-type code for astrophysical plasmas. The evolution of the plasma and magnetic field in the box is described by solving the full, time-dependent MHD equations for a resistive, fully ionized plasma, including gravity (for a curved loop), thermal conduction (including the effects of heat flux saturation), radiative losses from an optically thin plasma, and an anomalous magnetic diffusivity:

$$\frac{\partial \rho}{\partial t} + \boldsymbol{\nabla} \cdot (\rho \boldsymbol{v}) = 0, \tag{1}$$

$$\frac{\partial \rho \boldsymbol{v}}{\partial t} + \boldsymbol{\nabla} \cdot (\rho \boldsymbol{v}\boldsymbol{v}) = -\nabla \cdot (\mathbf{I}P + \mathbf{I}\frac{B^2}{8\pi} - \frac{\boldsymbol{B}\boldsymbol{B}}{8\pi}) + \rho \boldsymbol{g}, \tag{2}$$

$$\frac{\partial B}{\partial t} - \nabla \times (\boldsymbol{v} \times \boldsymbol{B}) = -\eta \nabla^2 \boldsymbol{B}, \tag{3}$$

$$\frac{\partial}{\partial t}\left(\frac{B^2}{8\pi} + \frac{1}{2}\rho v^2 + \rho\epsilon + \rho g h\right) + \nabla \cdot [\frac{c}{4\pi}\boldsymbol{E} \times \boldsymbol{B} + \frac{1}{2}\rho v^2 \boldsymbol{v} + \frac{\gamma}{\gamma - 1} P \boldsymbol{v} + \boldsymbol{F}_{\rm c} + \rho g h \boldsymbol{v}] = Q(T), \tag{4}$$

$$P = (\gamma - 1)\rho\epsilon = \frac{2k_{\rm B}}{\mu m_H}\rho T, \tag{5}$$

where t is the time, ρ is the mass density, $\boldsymbol{v}$ is the plasma velocity, P is the thermal pressure, $\boldsymbol{B}$ is the magnetic field, $\boldsymbol{E}$ is the electric field, $\boldsymbol{g}$ is the gravity acceleration vector for a curved loop, $\mathbf{I}$ is the identity tensor, ϵ is the internal energy, η is the magnetic diffusivity, T is the temperature, $\boldsymbol{F}_{\rm c}$ is the thermal conductive flux, $Q(T)$ includes the radiated energy losses and heating, m_H is the hydrogen mass density, $k_{\rm B}$ is the Boltzmann constant, and $\mu = 1.265$ is the mean ionic weight (relative to a proton and assuming coronal elemental abundances; E. Anders & N. Grevesse 1989);

The differential equations are numerically integrated with the MHD module available in PLUTO (A. Mignone et al. 2007), configured to compute intercell fluxes with the Harten–Lax–van Leer approximate Riemann solver (P. L. Roe 1986), while second-order accuracy in time is achieved using a Runge–Kutta scheme. A van Leer limiter (P. K. Sweby 1985) for the primitive variables is used. The solenoidal condition is maintained with the constrained transport approach (D. S. Balsara & D. S. Spicer 1999).

The equations are solved over a stratified, magnetized solar atmosphere, featuring a high-beta chromosphere at the opposite ends of the computational box, with a tenuous coronal environment in the middle, interfaced by a narrow transition region and threaded by multiple magnetic loop strands. Each strand is modeled as a straight coronal flux tube connecting the two chromospheric layers. The tube is much longer than it is wide, and except for the loop-aligned gravity, curvature effects are neglected. The chromospheric layers act as distant, independent loop footpoints.

We consider four interacting magnetic flux tubes, each with length 62 Mm, aspect ratio $\sim$10, and initial coronal temperature $\sim$1 MK. The coronal part of the strands is 50 Mm long, and everything else comprises the two TRs and chromospheric regions. The computational box is a 3D Cartesian grid, $-x_M < x < x_M$, $-y_M < y < y_M$, and $-z_M < z < z_M$, where $x_M = y_M = 7$ Mm and $z_M = 31$ Mm with a staggered grid, uniform along $\hat{x}$ and $\hat{y}$, with $\Delta x = \Delta y \sim 30$ km. Along $\hat{z}$, we use a nonuniform grid, with high resolution ($\Delta z \sim 25$ km) in the chromosphere and TR, while Δz logarithmically increases with height in the corona up to 100 km. The flux tubes extend along the z-direction and connect chromospheric layers placed at the top and bottom in this configuration.

To approach a semicircular configuration typical of coronal loops, we consider the gravity of the curved flux tube as follows (F. Reale et al. 2016; G. Cozzo et al. 2023):

$$g(z)\hat{z} = \begin{cases} g_\odot \sin\left(\pi \dfrac{z}{L}\right)\hat{z}, & |z| \leqslant 25 \text{ Mm}, \\ g_\odot \text{ Sign}(z)\,\hat{z} & |z| > 25 \text{ Mm}, \end{cases} \tag{6}$$

where $g_\odot = \frac{GM_\odot}{R_\odot^2}$ is the gravitational acceleration at the solar surface.

The thermal conductive flux is defined as follows:

$$\boldsymbol{F}_c = \frac{F_{\rm sat.}}{F_{\rm sat.} + |F_{\rm class.}|}\boldsymbol{F}_{\rm class.}, \tag{7}$$

$$\boldsymbol{F}_{\rm class.} = -k_\| \hat{\boldsymbol{b}}(\hat{\boldsymbol{b}} \cdot \boldsymbol{\nabla} T) - k_\perp [\boldsymbol{\nabla} T - \hat{\boldsymbol{b}}(\hat{\boldsymbol{b}} \cdot \boldsymbol{\nabla} T)], \tag{8}$$

$$F_{\rm sat.} = 5\phi\rho c_{\rm iso.}^3, \tag{9}$$

where $k_\| = 9.2 \times 10^{-7} T^{\frac{5}{2}}$, $k_\perp = K_\perp = 5.4 \times 10^{-16}\rho^2/(B^2 T^{\frac{1}{2}})$, $c_{\rm iso.}$ is the isothermal sound speed, $\phi = 0.9$ is a dimensionless free parameter, $\hat{\boldsymbol{b}} = \boldsymbol{B}/B$ is the magnetic field unit vector, and $F_{\rm sat.}$ is the saturated flux.

We account for optically thin radiative cooling in the corona with a rate per unit volume:

$$Q(T) = -\Lambda(T) n_e n_{\rm H} + H_0, \tag{10}$$

where $\Lambda(T)$ are the radiative rates per unit emission measure, while $n_{\rm H}$ and n_e are the hydrogen and electron number densities, respectively (see Appendix). The volumetric heating rate $H_0 = 4.3 \times 10^{-5}$ erg cm^{-3} s^{-1} is only used in the pre-avalanche phase to balance the initial energy losses and keep the loop in thermal equilibrium, and it is switched off when the avalanche starts, as the heating released by then is much higher. We use the optically thin radiative loss $\Lambda(T)$ values from the CHIANTI v. 7.0 database (E. Landi & F. Reale 2013), assuming coronal element abundances (U. Feldman 1992). To properly describe the plasma flows across the transition region (S. J. Bradshaw & P. J. Cargill 2013), we modeled the TR with an Adaptive Conduction method (TRAC; C. Johnston & S. Bradshaw 2019; C. D. Johnston et al. 2020, 2021).

We considered an anomalous plasma resistivity (A. Hood et al. 2009; F. Reale et al. 2016; G. Cozzo et al. 2023) that is switched on only in the corona and TR (i.e., above $T_{cr} = 10^4$ K) where the magnitude of the current density exceeds a threshold of

$$\eta = \begin{cases} \eta_0 & J \geqslant J_{cr} \text{ and } T \geqslant T_{cr} \\ 0 & J < J_{cr} \text{ or } T < T_{cr} \end{cases}, \tag{11}$$

where $\eta_0 = 10^{11}\,\mathrm{cm^2\,s^{-1}}$ and $J_{cr} = 300\,\mathrm{StC\,cm^{-2}\,s^{-1}}$ (allowing the buildup of strong currents in narrow current sheets and consequently their impulsive dissipation into heating). The minimum heating rate above the threshold is $H = \eta_0 4\pi J_{cr}^2/c^2 \approx 8 \times 10^{-5}\,\mathrm{erg\,cm^{-3}\,s^{-1}}$.

Each flux tube is rooted in the chromosphere, treated as a simple, thermally conducting, mass reservoir with no radiative losses. The magnetic field has a maximum strength of a few hundred Gauss in the chromosphere, and it expands into the corona to maintain total pressure equilibrium. The magnetic field has an amplitude of about 20 G in the corona and is line-tied to the upper and lower boundaries of the domain. In the model, magnetic tapering within the chromosphere results from the relaxation of an initially axial field, stronger around each flux strand (M. Guarrasi et al. 2014). The new equilibrium state is then used as the initial condition of the simulation. The initial atmosphere has a peak coronal temperature of 8×10^5 K, rapidly decreasing through the transition region to chromospheric temperature ($\sim 10^4$ K). The plasma density and pressure distributions are also analogous to those shown in M. Guarrasi et al. (2014), F. Reale et al. (2016), and G. Cozzo et al. (2023).

The boundary conditions (BCs) are periodic at $x = \pm x_M$ and $y = \pm y_M$. Reflecting BCs for the velocity and symmetric BCs for pressure and density were set at $z = \pm z_M$. The magnetic field is line-tied to the upper and lower boundaries (representing the dense, highly conducting chromosphere) and subject to equatorially symmetric BCs. Specifically, magnetic footpoints are anchored to these boundary planes, cannot slip relative to the plasma, and move according to prescribed boundary motions only.

Rotational motions at the upper and lower footpoint boundaries twist the flux tubes (similar to the setup of G. Cozzo et al. 2023 and F. Reale et al. 2016). The angular velocity $\omega(r)$ is constant (rigid-body-like) in an inner circle around the central axis of each strand, and then decreases linearly in an outer annulus (F. Reale et al. 2016),

$$v_\phi = \omega\, r \left[1 + 0.2\sum_{i=1}^{6} \sin(\phi\alpha_i)\, \sin\left(\frac{r}{r_{\max}}\alpha_i\right)\phi\right], \tag{12}$$

where α_i are random numbers between 0 and 30, different for each strand, and

$$\omega = \omega_0 \times \begin{cases} 1 & r < r_{\max} \\ (2r_{\max} - r)/r_{\max} & r_{\max} < r < 2r_{\max}. \\ 0 & r > 2r_{\max} \end{cases} \tag{13}$$

The four rotating regions have the same radius ($r_{\max} \sim 1$ Mm), but in one of them, the twisting velocity is 10% higher than in the others, reaching a maximum amplitude of $v_{\max} = 2.2\,\mathrm{km\,s^{-1}}$ ($\omega_0 = v_{\max}/r_{\max}$). This value corresponds to the peak rotational speed among the imposed footpoint drivers and is consistent with typical photospheric or chromospheric vortex motions observed in active regions (e.g., J. A. Bonet et al. 2008; K. Galsgaard & Å. Nordlund 1996). Such relatively slow rotational motions are commonly used in numerical models to emulate DC-type magnetic stressing (e.g., T. A. Howson & I. De Moortel 2022; C. D. Johnston et al. 2025), where the coronal field is gradually braided by persistent photospheric motions. In contrast, AC heating scenarios assume much faster, wave-like perturbations that excite MHD oscillations in the corona.

We run the simulation for a total duration of 6000 s, from $t = -2000$ s to $t = 4000$ s. The earlier evolution of the system, including the onset and development of the MHD avalanche process, has been described in detail in previous studies (G. Cozzo et al. 2023, 2024). In the present work, we focus instead on the subsequent phase driven by the continuous footpoint motions. We set the initial time ($t = 0$ s) immediately after the peaks of temperature, velocity, and current density during the avalanche (see Figure 2 in the following section). Consequently, negative times in the figures refer to the evolution before the kink instability and the avalanche event.

3. Results

3.1. Coronal Loop Evolution

At the beginning ($t = -2000$ s), the coronal loop is empty ($\rho < 2 \times 10^8\,\mathrm{cm^{-3}}$) and cold ($T < 1$ MK). The footpoint driver then twists each of the four flux tubes. The fastest-rotating strand becomes kink-unstable after 1000 s and fragments into a turbulent structure of thinner strands. The initial helical current sheet fragments into many narrow current sheets. The current sheets locally exceed the current density threshold for dissipation by anomalous resistivity (J_{cr} in Equation (11)), and there the magnetic field reconnects impulsively. Component-reconnection events occur intermittently across the guide magnetic field (B_z), producing localized bursts of heating and plasma acceleration. The resulting perturbations produced by the released magnetic tension propagate across the field lines, interacting with neighboring, still-stable flux tubes. This coupling triggers further small-scale energy releases, collectively forming a nanoflare storm. Here, we investigate what happens afterward, with sustained winding of the field lines, if and when a steady state is reached.

Figure 1 shows a 3D rendering of the simulation box at three different times, at the onset of the MHD avalanche ($t = -1000$ s), at its peak ($t = -740$ s), and after a relatively long time ($t = 1400$ s). The four flux tubes, subject to continuous footpoint twisting, are emphasized with field lines of different colors. In particular, in the top row, we show the atmospheric stratification of plasma density from one footpoint to the midpoint of the tube (corresponding to the loop apex in a curved geometry). The second and third rows display, respectively, the magnitude of the current density and the temperature distribution, both restricted to coronal heights ($|z| < 2$ Mm), where $T > 10^6$ K. At $t = -1000$ s, the loop bundles are already highly twisted and the onset of the kink instability is in the yellow strand, with a strong current and high-temperature shell enveloping the flux tube. The corona is still very tenuous ($n \sim 10^8\,\mathrm{cm^{-3}}$) and cold ($T \sim 0.8$ MK). At $t = -740$ s, the instability has propagated across the neighboring flux tubes. Reconnection occurs and the magnetic bundles lose their identity, as emphasized by the dispersed field lines. Chromospheric evaporation driven by the heating release starts to fill the corona with denser plasma (up to $10^9\,\mathrm{cm^{-3}}$) and large current sheets ($\sim 2000\,\mathrm{StC\,cm^{-2}\,s^{-1}}$ during the strands disruption), and high temperatures (peaks

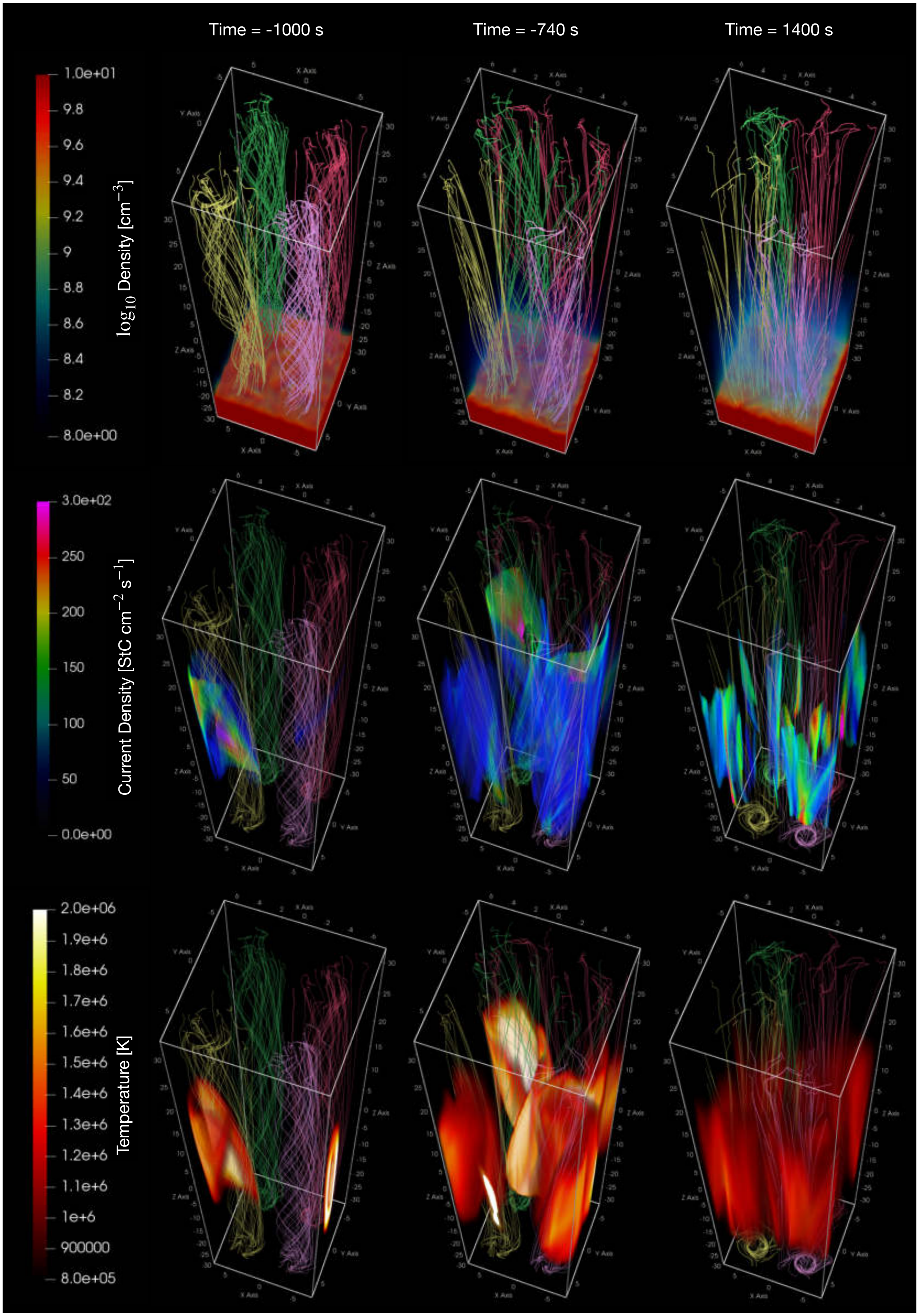

Figure 1. Three-dimensional rendering of a simulation of a coronal loop in a box at three time snapshots (before the avalanche, $t = -1000$ s; during the avalanche, $t = -740$ s; and after the avalanche, $t = 1400$ s). Colored field lines show the four magnetic field bundles subjected to continuous footpoint twisting. The first row shows the density stratification from the lower footpoint. The second row shows the current density magnitude in the corona. The third row shows the temperature distribution.

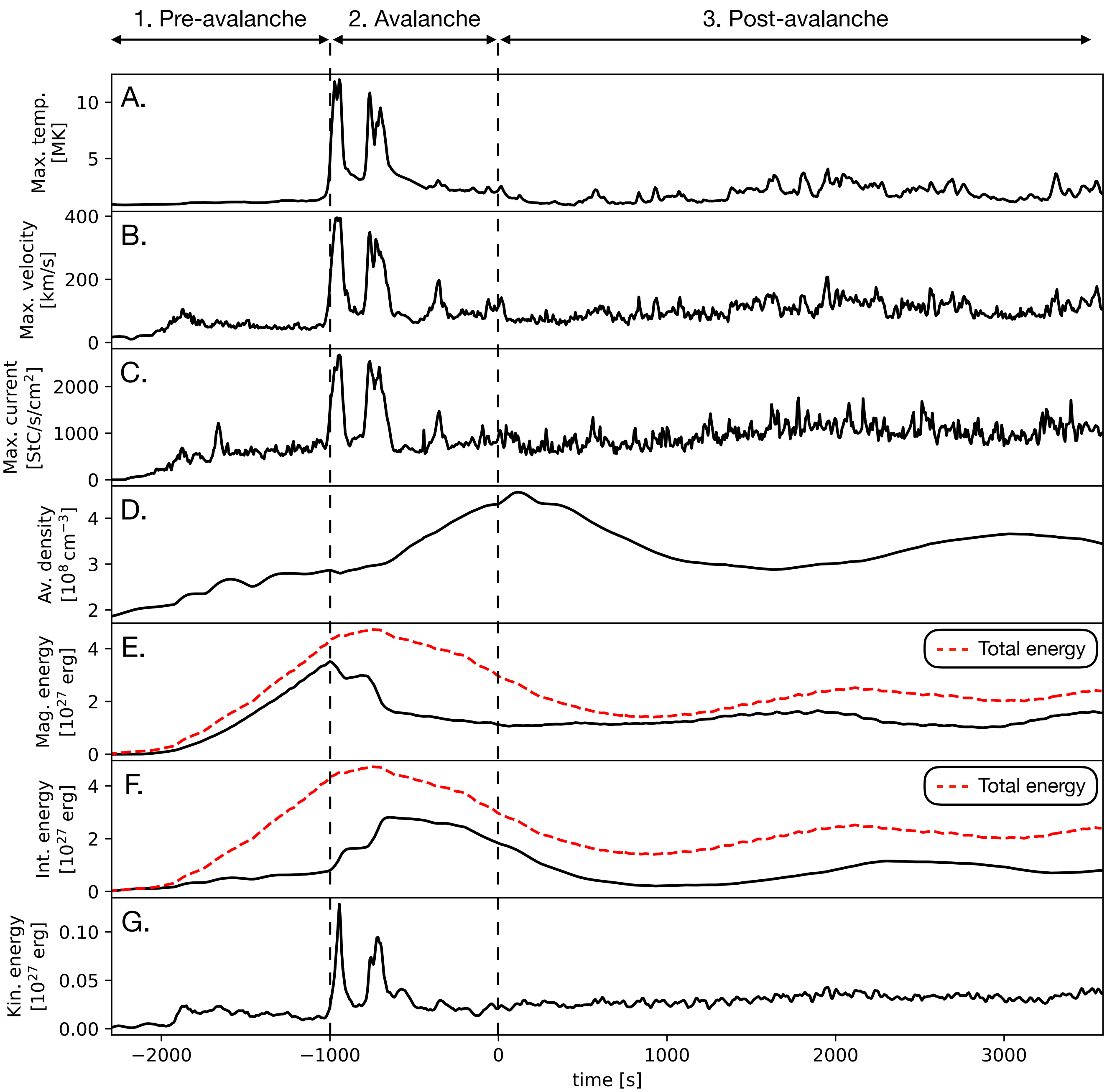

Figure 2. Long-term evolution of the bundle of four flux tubes. From top to bottom: Maximum temperature (A), maximum velocity (B), and maximum current density (C), average coronal plasma density ($T > 10^6$ K) (D), total magnetic (*E*), internal (*F*), and kinetic (*G*) energy as functions of time.

of 10 MK) spread throughout the coronal part of the box. At $t = 1400$ s, the coronal magnetic field has irreversibly fragmented into many bundles of field lines continuously reconnecting with each other. Indeed, with the driving progressing through time, field lines follow convoluted paths along the coronal loop length (magnetic braiding) corresponding to high magnetic stresses. Therefore, many narrow current sheets form in the corona and impulsively heat the plasma, with peaks in the temperature of ∼4 MK and an averaged value of ∼1.5 MK. The atmosphere reaches a statistical heat balance, with continuous footpoint twisting building up an excess of magnetic energy that is promptly released by DC heating events of nanoflare size.

Figure 2 summarizes the evolution of the simulation box from the initial, pre-avalanche twisting phase (phase 1, $t < -1000$ s), through the onset and rapid development of the instability (phase 2, $-1000 \leqslant t < 0$ s) and the following post-avalanche phase (phase 3, $t > 0$ s) for about 1 hr, which is longer than any typical timescale, e.g., sound-crossing time, Alfvén time, thermal conduction time, or radiative cooling time (F. Reale 2007).

In phase 1, temperature, density, and internal energy increase slowly and smoothly with time as the plasma is compressed in the twisted flux tube. The maximum velocity and the total kinetic energy (panels (B) and (G) in Figure 2) settle to a steady value, below 100 km s^{-1} and 5×10^{25} erg, respectively, due to impulsive reconnection events that release magnetic tension and accelerate the plasma (G. Cozzo et al. 2025). The maximum current (panel (C)) builds up linearly with time (with small spikes due to propagating waves), while

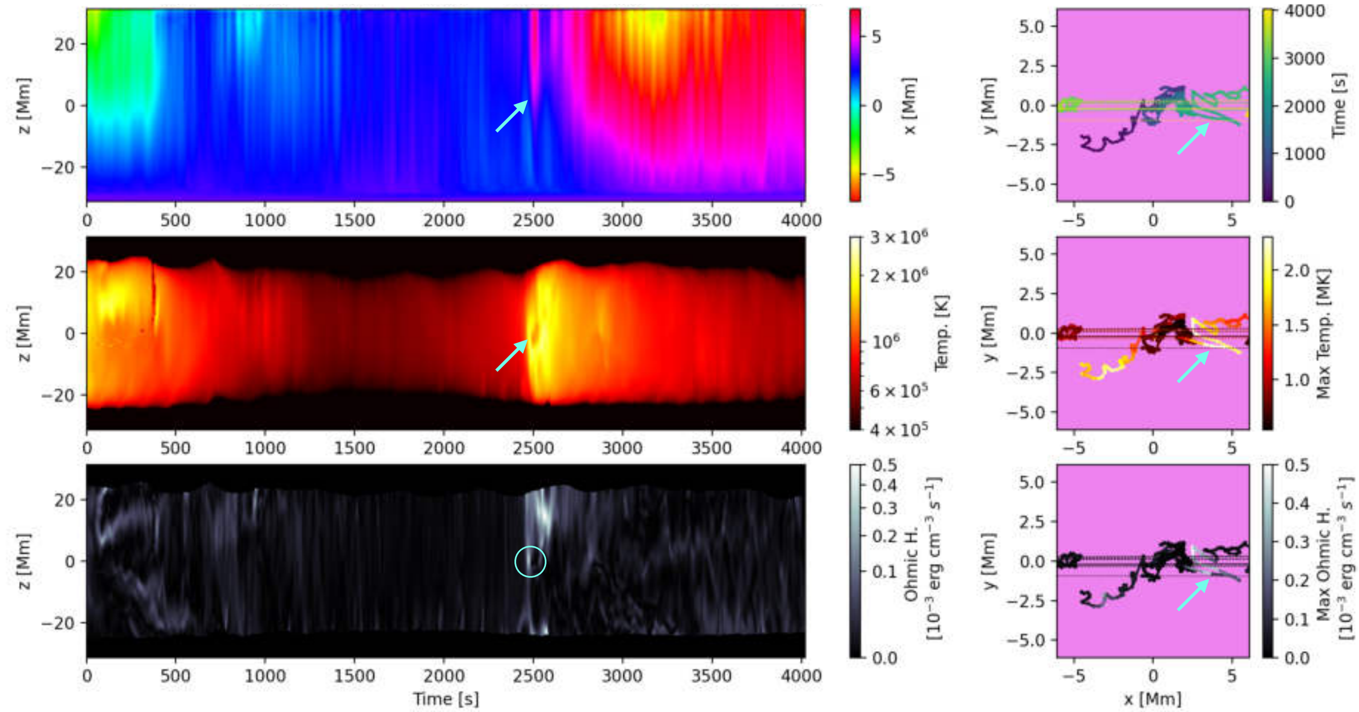

Figure 3. Evolution of a field line and the neighboring plasma. First row: the x-position of the field line along the loop length ($z = 0$ Mm is the apex) as a function of time (left), and the trajectory of the upper footpoint motion (the bottom footpoint moves following the footpoint driver). Second row: the distribution of the plasma temperature along the field line (left), and its maximum value (right). Third row: the distribution of the ohmic heating along the field line (left), and its maximum value (right). Cyan arrows and circle highlight a reconnection event.

the magnetic energy (panel (E)) shows a quadratic increase with time. Phase 2 is characterized by sudden sharp peaks of temperature (above 10 MK, panel (A)), velocity (above 300 km s^{-1}), electric currents, and kinetic energy, representing the disruption of the two couples of twisted strands at different times. The accumulated magnetic energy (panel (E)) drops dramatically by 50% in a few hundred seconds while the internal energy (panel (F)) increases by a similar amount. In particular, the conversion of $\sim 10^{27}$ erg into heat, together with the registered temperature peak of $\sim$10 MK, matches with the observations of microflares, such as those described by P. Testa & F. Reale (2020). The plasma density (panel (D)) starts to increase gradually via chromospheric evaporation during phase 2 and reaches its peak at $t \sim 0$ s, i.e., $\sim$1000 s after the strongest heat pulses, according to the typical flaring loop timescales (F. Reale 2007, 2014). After this density peak of about 4×10^8 cm^{-3}, the density, the magnetic energy, and the internal energy all settle to rather steady values, much higher than the initial ones, with smooth oscillations with a period of about 2000 s (phase 3). Also, the maximum temperature, velocity, current density, and kinetic energy settle around constant values, much lower than the initial peaks, with high-frequency rapid fluctuations, all corresponding to continuous, randomly distributed, reconnection episodes. Variations in the total energy (magnetic + internal + kinetic; red and dashed lines in panels (E) and (F)) are stronger during phase 1, when the magnetic strands load magnetic energy in excess, and in the first $\sim$2000 s after the avalanche, when the thermal energy converted during the avalanche is radiated away. Kinetic energy is always negligible compared to the other two contributions, and it is strongest during the avalanche.

3.2. Reconnection Signatures

One of the main goals of this study is to explore the reconnection details when the system has reached a steady state, in a rather dense and chaotic environment. We now focus on the evolution of a single field line subject to reconnection.

Figure 3 shows features of the temporal evolution of a selected field line. The line is retrieved by using a fourth-order Runge–Kutta scheme, and starting from a point in the lower boundary. We follow the motion of the starting point according to the footpoint driver and reconstruct the field line from each position during the motion. The time–distance maps show, from top to bottom (left), the position of the field line in the x-direction, the temperature, and the ohmic heating. The motion of one (the uppermost) of the field line footpoints is shown on the right. The three quantities show a behavior alternating smooth evolution with rapid changes corresponding to sporadic and localized heating events and reconnection.

The three quantities all follow a similar, irregular behavior. For extended periods, the field line drifts only slightly as the boundary driving slowly twists its footpoints, the temperature hovers near the coronal background of about 1 MK, and the ohmic heating sits close to zero. Every so often, however, the curve shows sudden sideways jumps of megameter size. These jumps coincide with equally sharp spikes in J^2/σ and brief temperature rises of a few million degrees kelvin.

For instance, the rapid variations (change in color) in time, around $t \sim 2500$ s, indicate a reconnection event (also visible as a long track in a short time in the right plot) occurring close to the loop apex ($z = 0$ Mm), as marked by the arrows and circle. The field line breaks around $z = 0$ Mm, and the lower half joins another line. In the figure, the upper half of the line suddenly jumps into another footpoint. The second and third

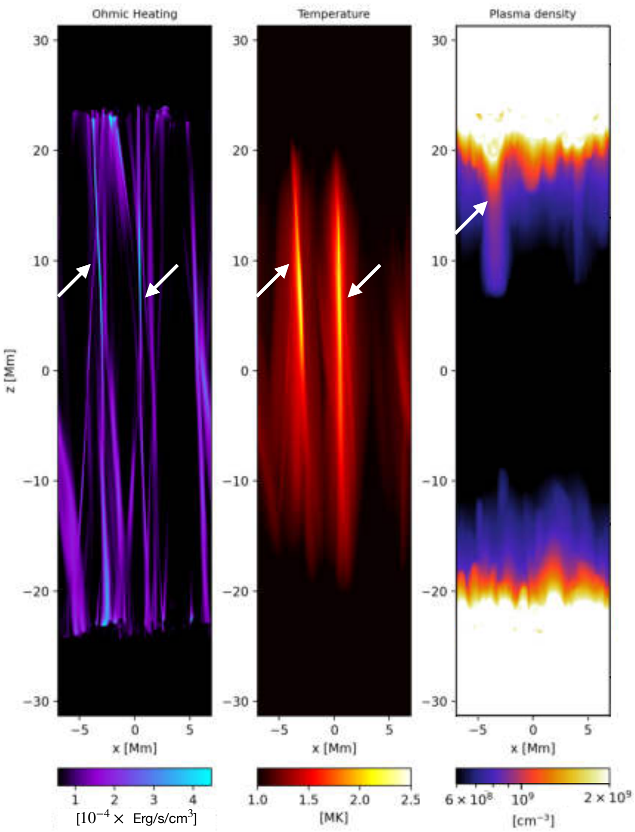

Figure 4. Current sheets along the flux tube. The panels show maps of the distribution of maximum ohmic heating and temperature (along the $\hat{y}$ direction), and a cut of the plasma density across the box at time ∼3000 s after the onset of the instability. White arrows in the first and second panels point at the location of two current sheets, while in the third panel an upflow of plasma evaporating from the TR is shown.

rows report rapid variations in temperature and strong, localized electric currents when reconnection occurs. Specifically, the reconnection leads to a significant heating release (circle) and a temperature increase (arrow) from 1 MK to about 3 MK. In the right-hand panels, regions of elevated temperature and enhanced heating rate coincide with the upper footpoint jumps, namely the abrupt connectivity changes produced by magnetic reconnection. After the heating event, the flux tube cools down again, below 1 MK, due to radiation and thermal conduction. In particular, when the heating is localized and the plasma density initially small, the timescale for cooling by thermal conduction ($< \rho\epsilon/|\nabla \cdot \boldsymbol{F}_c| > \approx 80$ s, with $T \approx 3$ MK and $n \approx 10^8$ cm^{-3}) dominates the early decay of the heated plasma, while radiative cooling becomes important only during the later, lower-temperature/higher-density phase ($\tau_{\rm rad} = < \rho\epsilon/Q(T) > \sim 3k_{\rm B}T/[n\Lambda(T)] \approx 1200$ s, with $T \approx 1$ MK and $n \approx 10^9$ cm^{-3}; F. Reale 2007, 2014). Reconnection events can drive reconnection outflows (G. Cozzo et al. 2025; S. Sen & F. Moreno-Insertis 2025): the rejoined field lines rapidly relax, pushing the plasma sideways, perpendicular to the guide magnetic field (P. Antolin et al. 2021). The field expansion from the reconnection region and the compression of the surrounding magnetic field can further assist local increases or decreases in temperature. The expansion/contraction timescale ($\tau_{\rm ad} = \Pi^{-1}$, with $\Pi = -(\gamma - 1)\nabla \cdot \boldsymbol{v}$; J. Hermans & R. Keppens 2021; S. Sen & F. Moreno-Insertis 2025) in our simulation can be as short as ∼200 s inside reconnecting current sheets, to be compared with the minimum ohmic heating timescale $\tau_{\rm ohm} = \epsilon/(4\pi\eta_0 J^2/c^2) \sim 100$ s.

Figure 4 shows maps at time ∼3000 s of the coronal flux tube during the impulsive dissipation of two current sheets. The map of the maximum ohmic heating rate (left panel) shows two main bundles of current sheets, where energy release is stronger than the surroundings and confined in a limited range of height around $z \sim 10$ Mm. This corresponds to two strips of higher temperature (middle panel), up to about 2.5 MK. As expected, little direct evidence of the heating release can be found in the density map (right panel). There is a hint of evaporation around and above the transition region (arrow), at the footpoint corresponding to one of the strongest current sheets.

3.3. Forward Modeling

We have synthesized observable quantities from the simulation as described in G. Cozzo et al. (2024). Instrument temperature response functions are calculated using CHIANTI 10 (G. Del Zanna et al. 2021), considering ionization equilibrium, coronal element abundances (U. Feldman 1992), constant electron density (10^9 cm^{-3}), and no absorption. We used the whole band of each filter to synthesize AIA images (P. Boerner et al. 2012). We also accounted for AIA instrumental point spread functions (PSFs; B. Poduval et al. 2013), while for MUSE PSFs, we considered a Gaussian with an FWHM of 0.″45. Emission was then rebinned at the instruments' respective pixel sizes (0.″6 for AIA and 0.″167 for MUSE).

In Figure 5, we present synthetic AIA emission maps at the same time as in Figure 4. Each panel displays a side view of the intensity distribution integrated along the line of sight in the six EUV channels (P. Boerner et al. 2012). In all channels except for 131 Å and 335 Å, we see diffuse emission along the entire coronal section of the flux tubes. In the 193 Å and 211 Å channels, we see bright filamentary structures at the location of the hot plasma filaments shown in Figure 4. In the 94 Å and 171 Å channels, we see bright spots just above the TR, corresponding to the footpoints of reconnected field lines. While the emission in the 193 Å and 211 Å channels is due to the temperature enhancement in hot strands, the bursts observed at 94 Å and 171 Å are caused by the density increase, as chromospheric plasma expands in response to the deposition of heat in the lower atmosphere.

The online animated version of Figure 5 shows the evolution of the emission in the six AIA channels. The initially hot (∼2.5 MK) coronal flux tube is bright at 193 Å. After 400 s, it cools down to ∼1 MK, growing fainter in the 193 Å filter and brightening in the 94 Å and 171 Å channels. The emission in those channels is higher in the lower corona and relatively uniform in the cross-field direction. Between $t = 1000$ s and $t = 2000$ s, the atmosphere is faint in all the AIA channels: this is the period where both plasma density and internal energy show a dip in the time profiles shown in Figure 2. A secondary, post-avalanche, collective energy release is registered starting from $t = 2000$ s. This is the outcome of several small-scale heating events visible as narrow strips both in the 193 Å and 211 Å channels.

Figure 6 shows a side view of the flux tube emission, Doppler shift along the line of sight, and nonthermal line broadening in the MUSE Fe IX line at 171 Å and Fe XV at 284 Å at the same

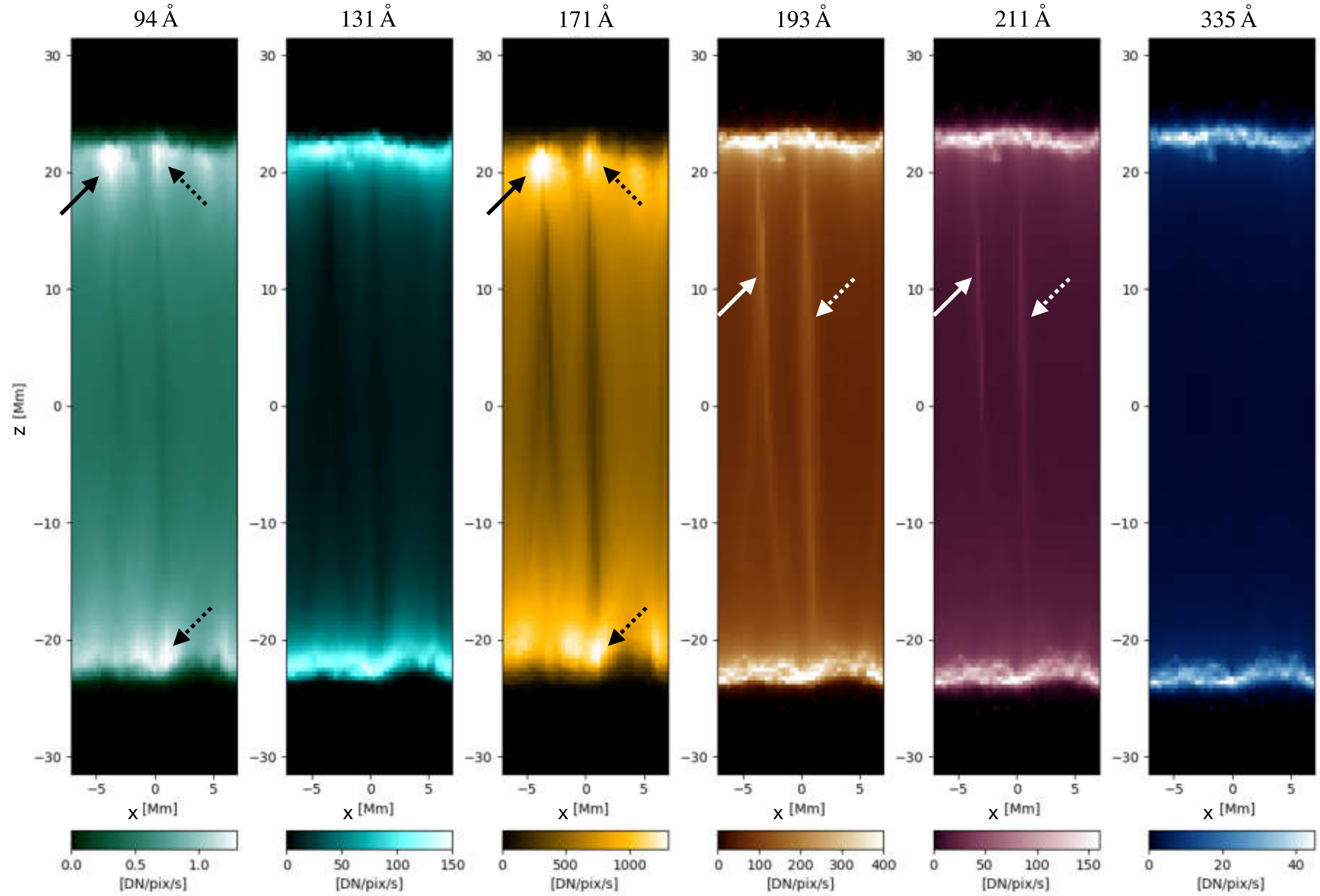

Figure 5. AIA synthetic maps, from the PLUTO 3D MHD simulation of the multithreaded magnetic flux tube discussed in Section 2, at time ∼3000 s after the onset of the instability and with the loop in the off-limb configuration (LoS along the $\hat{y}$ direction). From the left, intensity in the 94 Å, 131 Å, 171 Å, 193 Å, 211 Å, and 335 Å channels, respectively. Arrows indicate the brightenings due to impulsive heating events. An animation in the online Journal shows the temporal evolution of the six panels, across the six optically thin channels of AIA. The animation is 90 s in duration, covering t = 0–4155 s of the simulation.

(An animation of this figure is available in the online article.)

snapshot as in Figures 4 and 5. The Doppler velocity (I_1) and the nonthermal width (I_2) in each channel are computed as the first and second moments of the velocity distribution, weighted for the emissivities, as described in G. Cozzo et al. (2024) and B. De Pontieu et al. (2022), and in Equations (14) and (15):

$$I_1 = \frac{\sum_k F_k \Delta_k v_k \Delta_k}{I_0}, \tag{14}$$

$$I_2 = \sqrt{\frac{\sum_k F_k \Delta_k (v_k - I_1)^2}{I_0}}, \tag{15}$$

where F_k is the emission of the kth bin (with pixel width Δ_k), summing along $\hat{k}$ yields the total line intensity I_0, and v_k is the plasma velocity. For comparison, the thermal widths of the Fe IX and Fe XV lines, at their peak temperatures, are ∼26 km s^{-1} and ∼46 km s^{-1}, respectively. The MUSE Fe IX emission closely resembles that of the AIA 171 Å channel, including similarly brightened footpoints, as indicated by the arrows. The Doppler-shift map shows an alternating pattern of red- and blueshifted velocity, at magnitudes up to about 20 km s^{-1}, organized into elongated, thin strands. These slow Alfvénic and tortional motions captured by the cold channel do not show strong correlation with any impulsive heating event, although their oscillating behavior is likely powered both by the footpoint driver and the residual dynamics released in the corona during reconnection. Likewise, the line broadening exhibits a filamentary structure punctuated by localized regions with significant broadening (up to ∼25 km s^{-1}). Conversely, emission in the MUSE 284 Å line is bright only within two very narrow strips, clearly traceable back to the locations of heating deposition described in Figure 4, and correlating with the bright footpoint spots observed in the AIA 193 Å and 211 Å channels. The Doppler-shift maps in the MUSE 284 Å line distinctly capture bidirectional outflows from the locations of peak brightness. Additionally, the line broadening appears to be the strongest in the core of the emission regions, as compared to their surroundings.

The online, animated Figure 6 shows the evolution of emission, Doppler velocity, and nonthermal line broadening in the MUSE Fe IX and Fe XV channels. Fe IX emission here evolves in a manner analogous to that in the AIA 171 Å filter, although the enhanced resolution allows the detection of small-scale, cross-field structuring. The Doppler velocity shows alternation of blue- and redshifted regions, while the

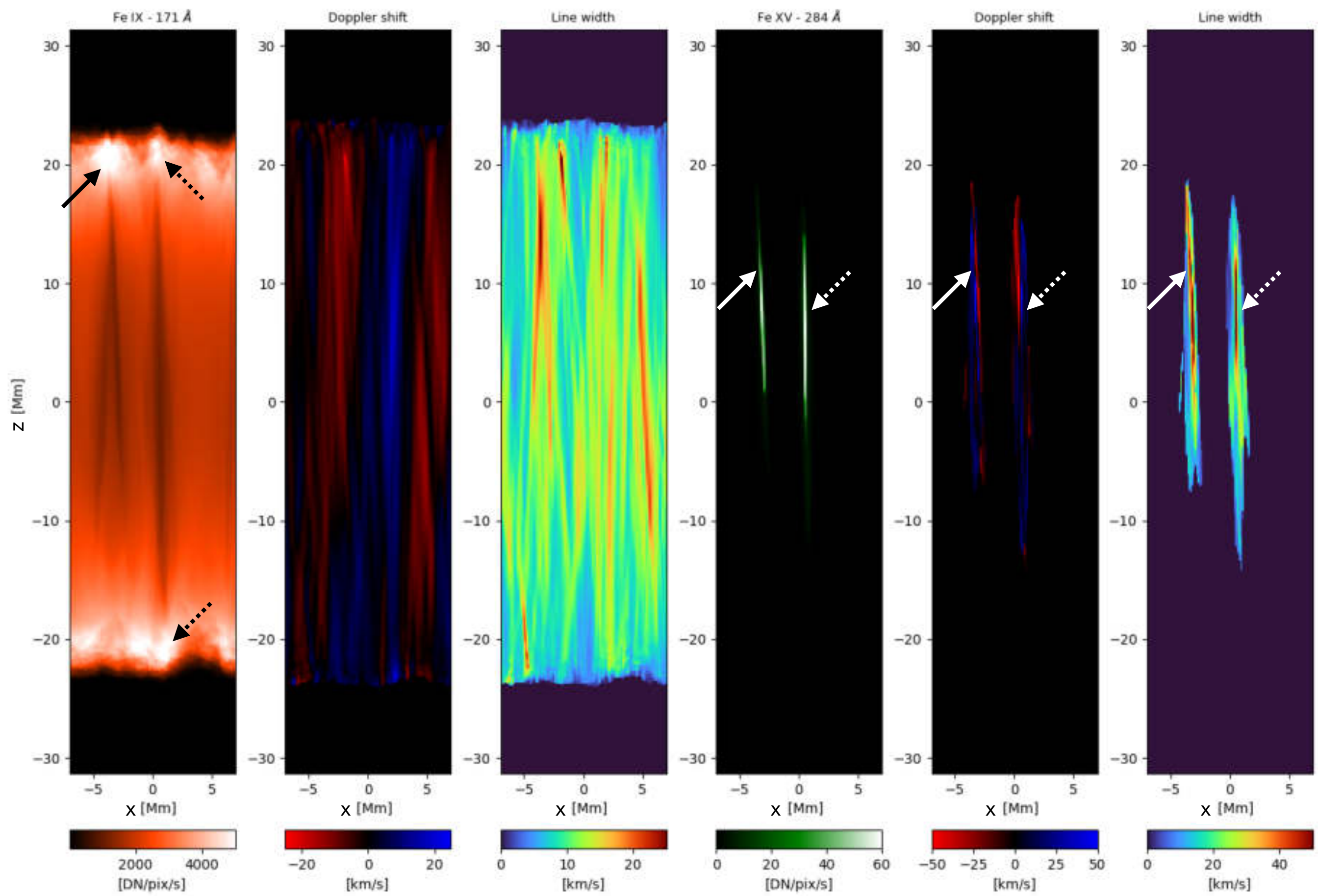

Figure 6. MUSE synthetic maps, from the PLUTO 3D MHD model of the multithreaded magnetic flux tube discussed in Section 2. Here, we show the tube structure at time ∼3000 s after the onset of the instability and with the loop in the off-limb configuration (LoS along the $\hat{y}$ direction). From the left, the panels show the intensity, Doppler shifts, and nonthermal line broadenings of the Fe IX 171 Å and Fe XV 284 Å emission lines. Arrows indicate the brightenings due to impulsive heating events. An animation in the online Journal shows the temporal evolution of the six panels, across the Fe IX and Fe XV channels of MUSE. The animation is 90 s in duration, covering t = 0–4155 s of the simulation.

(An animation of this figure is available in the online article.)

Table 1
Simulation Parameters and Corresponding Lundquist Numbers

Sim.	B (G)	η (cm^2 s^{-1})	J_{cr} (StC cm^{-2} s^{-1})	Δ (km)	S
1	20	10^{11}	300	25	3.5×10^3
2	10	10^{11}	150	25	1.8×10^3
3	10	10^{13}	150	25	1.8×10^1
4	10	10^{11}	150	50	3.5×10^3

nonthermal width appears filamented, with subarcsec structuring across the guide field. Fe XV brightens up only sporadically within fine strips, always accompanied by strong enhancement in the nonthermal line broadening and Doppler shifts marking bidirectional outflows departing from the bright spots.

3.4. Effects of Magnetic Diffusivity on Heating

To investigate the role of dissipation, we performed three additional simulations. We considered a guide magnetic field of 10 G, we varied the magnetic diffusivity (η) between 10^{11} and 10^{13} cm^2 s^{-1}, and we varied the smallest spatial cell width (Δ) between 25 km and 50 km, as summarized in Table 1. The current density threshold is chosen to scale with the intensity of the magnetic field (150 StC cm^2 for B = 10 G, 300 StC cm^2 for B = 20 G), in order to generate current sheets of similar thickness. For the adopted plasma parameters (assuming $n = 10^9$ cm^{-3}), the Lundquist number spans from ($S \sim 10^1$) in run 3 to ($S \sim 10^3$–10^4) in the other cases (Table 1). These values indicate that magnetic reconnection proceeds in a moderately resistive regime. Runs 1, 2, and 4, with ($S \gtrsim 10^3$), lie close to the threshold ($S \sim 10^4$–10^5) at which the plasmoid instability can begin to fragment current sheets into multiple secondary islands, leading to bursty, turbulent reconnection. In contrast, run 3 (with the higher resistivity and $S \sim 10^1$) falls well below this threshold and is expected to exhibit laminar, Sweet–Parker-like reconnection.

In Figure 7, we explore how magnetic diffusion influences the formation, morphology, and strength of the current sheets generated by the magnetic field shear, which subsequently dissipate into heat due to anomalous resistivity. Specifically, the histograms in the first column show the distribution of the minimum current sheet thickness (λ_B) at each temporal output, for runs 2 to 4. The current sheets develop mostly along the strong guide field in the $\hat{z}$-direction. We estimate the characteristic thickness of these thin layers via the ratio between the magnitude of the transverse ("component") magnetic field, $|b| = \sqrt{b_x^2 + b_y^2}$ (lying in the $\hat{x}$–$\hat{y}$ plane,

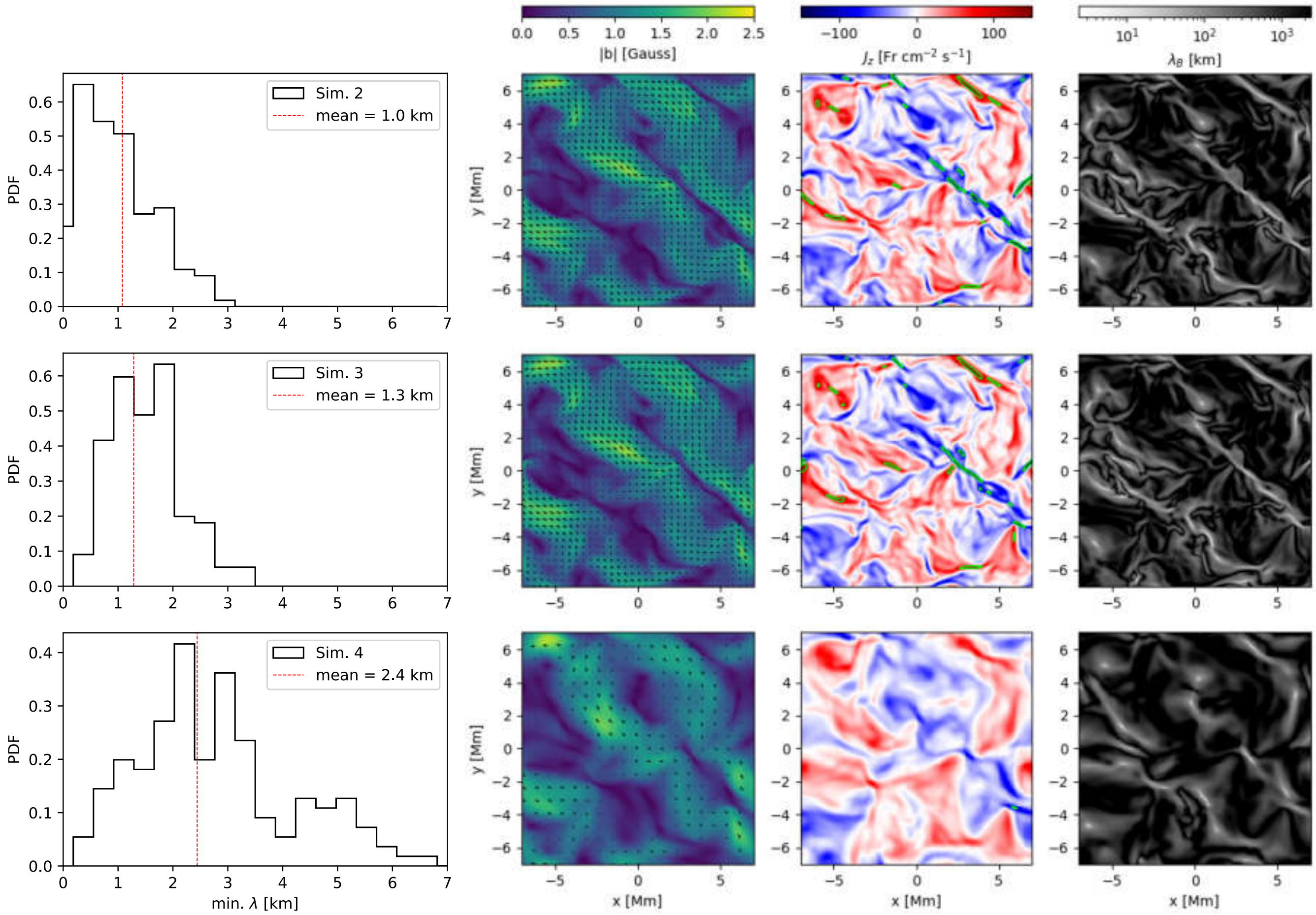

Figure 7. Effects of magnetic diffusion on current sheets. Left: The histograms of the distributions of the minimum current sheets thickness ($\lambda_B = \frac{c}{4\pi}|b|/|J_z|$) for simulations 2, 3, and 4, listed in Table 1, with different resolutions ($\Delta_{\min} = 25$, 50 km) and levels of magnetic diffusion ($\eta = 10^{11}$, 10^{13} cm^2 s^{-1}). Right: The maps of the horizontal magnetic field (second column), vertical current density (third column), and λ_B (fourth column) distribution on a horizontal cut at the midplane, ∼1500 s after the onset of the avalanche, for each of the three simulations.

second column of Figure 7), and the magnitude of the current density along $\hat{z}$ (J_z, third column),

$$\lambda_B = \frac{c}{4\pi}\frac{|b|}{|J_z|}. \tag{16}$$

An example of the distribution of λ_B at the midplane of the box (loop apex) is shown in the fourth column. Simulation 2 (first row in Figure 7) is the least current-dissipative because it has both the smallest magnetic resistivity and the highest resolution, as compared with runs 3 (higher η) and 4 (lower resolution). Increasing the magnetic diffusivity in run 3 (second row in Figure 7) results in a larger average thickness of the current sheets, with the effect being significantly more pronounced when the numerical diffusivity is higher due to the coarser spatial grid, as in run 4 (third row in Figure 7).

We now examine how the intensity distribution of the heating depends on magnetic field strength, magnetic diffusivity, and spatial resolution. The left panel in Figure 8 shows the time-averaged probability density functions (PDFs) of the square of the current density (proportional to the volumetric ohmic heating rate $E = J^2/\sigma$), i.e., the fraction of the volume $V(J^2)$ where the local heating rate falls within each (logarithmic) current density bin. The curves in the right panel show the same quantity multiplied by the respective current density square, as an estimate of the ohmic energy carried by each current bin. Transparent regions mark subcritical currents ($J < J_{\rm cr}$) where no heating from anomalous magnetic diffusivity is occurring. The left PDFs show that the occurrence frequency in the heating regime closely follows a power law $\propto E^{-1.8}$ expected for a nanoflare distribution (H. Hudson 2010). The right PDFs show a rather flat energy contribution across the inertial range, such that no single scale dominates the total heating budget. Deviations at the lowest energies are set by the numerical diffusion floor, while the high-energy cutoff reflects the finite magnetic free energy reservoir. Together, the PDFs show that threshold-triggered dissipation not only localizes heating to strongly current-bearing strands but also reproduces the expected statistical signatures (both in event counts and in energetic impact) of nanoflare-driven coronal heating. Generally, electric currents tend to accumulate until reaching the threshold for anomalous dissipation, as illustrated by the current-density-weighted PDFs (right). As expected, a stronger magnetic field results in more intense heating (Sim. 1 versus Sim. 2). Conversely, a lower spatial resolution inhibits the buildup of currents, significantly reducing the amount of heating released. Higher magnetic diffusivity, as in Sim. 3, dissipates magnetic stresses more efficiently, thereby suppressing the formation of intense current sheets, as shown by the increasing distance between

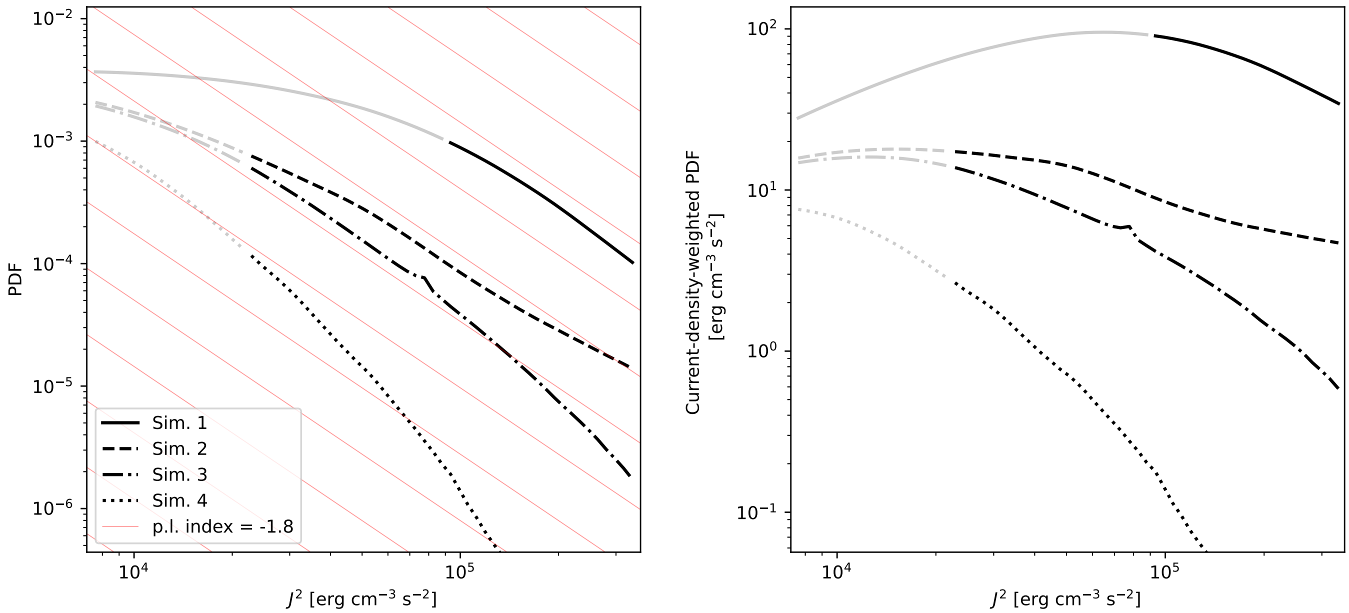

Figure 8. Effects of magnetic diffusion on the heating. In the left panel, we show the time-averaged PDFs of the current density square (proportional to the volumetric ohmic heating rate) for four numerical runs with respective magnetic field strengths 10 G and 20 G, minimum spacings $\Delta = 25$ km and 50 km, and magnetic diffusivities $\eta = 10^{11}$ and 10^{13} cm^2 s^{-1}. Specifically, opaque regions mark heating from anomalous dissipation ($J > J_{cr}$), while lighter regions still show the J^2 distribution, which the code does not explicitly dissipate (but which may be subject to numerical diffusion). The red lines mark a reference power law with index -1.8, illustrating the canonical nanoflare-size distribution expected for impulsive heating events in the solar corona. Similarly, on the right, we show the current-density-weighted PDFs.

the dashed (Sim. 2) and dotted–dashed (Sim. 3) curves at high values of J^2.

4. Discussion and Conclusions

In G. Cozzo et al. (2023), we explored how kink-unstable flux tubes fragment into chaotic current sheets where magnetic reconnection triggers impulsive heating release, through anomalous resistivity, in the presence of a stratified atmosphere from the chromosphere to the corona. The faster-rotating flux tube fragments first and propagates the instability to the other slower one, thus describing an avalanche process that might explain the ignition of a larger-scale coronal loop. The initial heat pulses in a relatively empty atmosphere lead to strong local temperature peaks (up to about 10 MK), before evaporation fronts bring up dense plasma to fill the corona. It is then interesting to investigate what happens on a longer timescale with continuous driving of the twisting, in particular if and what steady-state conditions are reached, and then what is the dependence of these conditions on some crucial parameters. Specifically, we ask whether the magnetic field remains capable of storing the energy continuously provided by footpoint motions, ultimately triggering nanoflare storms, or if the accumulated energy is quickly released through frequent but less energetic nanoflares (A. Rappazzo et al. 2013).

To address these questions, the stratified atmosphere (G. Cozzo et al. 2023) is important because it allows us to accurately study the plasma response to the impulsive heating in the corona and chromosphere, and it is used in forward-modeling both existing (e.g., AIA/SDO and IRIS) and forthcoming (MUSE) observations (G. Cozzo et al. 2023).

Also in this work, we consider three-dimensional MHD simulations of an MHD avalanche occurring within a kink-unstable, multithreaded coronal loop system (see also A. W. Hood et al. 2016; J. Reid et al. 2018, 2020; G. Cozzo et al. 2023). At variance with the previous work, here we consider four, instead of two, thinner magnetic flux tubes. The critical amount of twist for kink-instability is therefore smaller (A. Hood & E. Priest 1979), and the four initial strands get fragmented in a shorter period of time. As before, they are embedded in a stratified atmosphere, characterized by a corona at 1 MK anchored on both ends to a denser, cooler (10^4 K) isothermal chromosphere. Rotational motions at the loop footpoints progressively twist these flux tubes in an ambient magnetic field of strength $B_{bkg} = 20$ Gauss. A small anomalous magnetic resistivity (10^{11} cm^2 s^{-1} and J_{cr}) facilitates the buildup of strong currents in narrow current sheets, making the heating impulsive and localized.

As twisting continues, the flux tubes become kink-unstable and rapidly fragment into a chaotic structure filled with thin current sheets, hosting small-scale impulsive reconnection events. In particular, the two pairs of flux ropes merge by magnetic reconnection at different times (P. Browning & E. Priest 1986). These events locally and impulsively heat the plasma to peak temperatures exceeding 10 MK as soon as the instability propagates. The widespread intense nanoflares also trigger chromospheric evaporation, thereby enhancing loop brightness in the EUV band (G. Cozzo et al. 2024).

We follow the evolution of the system for over 1 hr after the avalanche is triggered, longer than typical cooling times. In our model, continuous driving motions at the loop footpoints (F. Reale et al. 2016; J. Reid et al. 2018) consistently inject magnetic energy into the corona. Consequently, the pre-fragmented magnetic field configuration naturally facilitates the formation of additional current sheets, as well as sustained ohmic dissipation through anomalous resistivity. Specifically, the coronal loop remains endlessly braided, undergoing intermittent episodes of resistive relaxation. Its tangled magnetic field triggers spontaneous reconnection, producing a cascade of small-scale nanoflares (D. Pontin et al. 2011).

Eventually, the system gets to a balance between radiative losses, thermal conduction, and continuous coronal DC heating, and a statistical steady-state equilibrium is established (J. Reid et al. 2020). Following each reconnection event, the field attempts to relax toward a lower-energy configuration, yet the continuous application of driving velocities, leading to sustained injection of energy from boundary motions, prevents the magnetic system from approaching the minimal-energy state predicted by classical relaxation theory (J. B. Taylor 1974). Temperature and current density are highly structured at subobservational scales, making the loop plasma multithermal, with dynamic current strands scattered throughout. Consequently, coronal heating is found to be highly intermittent, with most of the loop cooling at any given time (R. Dahlburg et al. 2016).

Previous studies have proposed that current sheets can form with sufficiently tangled magnetic fields driven by complex boundary motions (D. Hendrix & G. Van Hoven 1996; C. Ng et al. 2012). In this scenario, the relatively simple vortex motions imposed at the boundaries lead to initially distinct and coherent magnetic flux tubes. Nevertheless, the onset of instability leads to significant changes in magnetic connectivity. As a consequence, magnetic field lines become linked to different vortices, and the ongoing twisting boundary motions begin to braid the field lines into an increasingly complex configuration. Therefore, current sheets spontaneously emerge from a highly ordered initial state, with sustained footpoint motions gradually braiding the magnetic field, a phenomenon frequently observed in similarly driven simulations (A. Wilmot-Smith 2015; J. Reid et al. 2018, 2020).

Figure 2 clearly shows the initial breakup that determines peaks of temperature around 10 MK, in agreement with G. Cozzo et al. (2023). Afterward, both the gradual filling of the tubes by chromospheric evaporation, which determines an increase of the plasma heat capacity, and the continuous energy release, which inhibits large energy accumulation for strong events, prevent the loop plasma from reaching the initial high-temperature peaks; instead, the loop shows a continuous sequence of smaller peaks. These subsequent heating events exhibit neither clear periodicity nor characteristic magnitude (J. Reid et al. 2020). Average temperature and density achieved by the system at regime are comparable with the results found by T. A. Howson & I. De Moortel (2022) with a guide field strength of 20 G.

The synchronized signatures of current density and temperature mark clear reconnection pulses (Figure 3): field lines reconnect through narrow current sheets, their magnetic connections rearrange almost instantaneously, and the stored magnetic energy is dissipated locally as heat. Once the burst is over, the plasma cools via conduction and radiation, and the line settles back into its slow drift until the next trigger. This alternation of gradual buildup and rapid release is the textbook pattern expected for nanoflare-style heating of coronal loops.

G. Cozzo et al. (2025) demonstrated that the detection of localized heating events is facilitated by examining the emission of narrow, hot spectral lines (e.g., MUSE Fe XIX 108 Å), as compared to broadband AIA channels such as 94 Å, in which emission from hot lines is blended with cooler background emission (e.g., A. R. Foster & P. Testa 2011; F. Reale et al. 2011; P. Testa & F. Reale 2012; P. Testa et al. 2012; G. Del Zanna 2013). Though in a different regime, a similar conclusion can be drawn from the present work by comparing the emission maps of the MUSE Fe XV 284 Å line with synthetic emission images derived from the AIA 193 Å and 211 Å channels.

As illustrated in Figure 6, in the regime of our first simulation, the average temperature here settles to approximately 1 MK, punctuated by temperature spikes around 2.5 MK in transient and bright strands (C. Breu et al. 2022), so the Fe IX 171 Å line emission is dominated by background emission from cooling plasma (with bright spots at the footpoints), whereas the Fe XV 284Å line emission clearly highlights localized heating events.

In this paper, we also explored various conditions of resistivity and resolution (see Table 1). Smaller resistivity and higher grid resolution lead to strong currents (Figure 8) in finer sheets (Figure 7), as reduced (physical and numerical) dissipation allows stresses to build up to higher levels (A. F. Rappazzo et al. 2007; A. Rappazzo et al. 2008). Stronger currents lead in turn to more intense heating events (Figure 8), described with a frequency–energy power law with index ∼−1.8, in agreement with the "flare syndrome theory" (H. Hudson 2010) and supported by numerous observations at higher energies (J. F. Drake 1971; B. R. Dennis 1985; N. B. Crosby et al. 1993).

In conclusion, in this work, we verified that, after an impulsive transient due to the onset of the kink instability, on long timescales, a continuous footpoint driver of a multiple flux tube system leads to an almost steady-state regime. The frequent power-law-distributed nanoflares heat the plasma to lower temperatures than in the transient and keep the system at a 1 MK regime with the selected background magnetic field, with interesting implications for the observables. We have also confirmed that the diffusion and resolution parameters are important in determining the intensity of the bursts. Future investigations will explore different regimes, for instance those of active regions.

Acknowledgments

G.C. and P.T. were supported by contract 4105785828 (MUSE) to the Smithsonian Astrophysical Observatory, and by NASA grant 80NSSC21K1684. B.D.P. and J.M.S. were supported by NASA contract 80GSFC21C0011 (MUSE) and NNG09FA40C (IRIS). G.C., P.T., J.M.S., and V.H. were supported by NASA contract 80NSSC26K0018. P.P., and F.R. acknowledge support from ASI/INAF agreement n. 2022-29-HH.0. This work made use of the HPC system MEUSA, part of the Sistema Computazionale per l'Astrofisica Numerica (SCAN) of INAF-Osservatorio Astronomico di Palermo. The simulations have been run on the Pleiades cluster through the computing projects s1061, s2601, from the High-End Computing (HEC) division of NASA. We acknowledge the CINECA award under the ISCRA initiative, for the availability of high-performance computing resources and support.

Software: PLUTO (A. Mignone et al. 2007).

Appendix
Radiative Losses

Atmospheric gravitational stratification on the Sun is modulated by radiative and heat transfer. In the corona, collision de-excitation and photon absorption are negligible, so generated photons directly escape. Optically thin radiative cooling is important in the corona, with a rate per unit volume of

$$Q_{\rm coro} = n_{\rm H} n_{\rm e} \Lambda(T), \tag{A1}$$

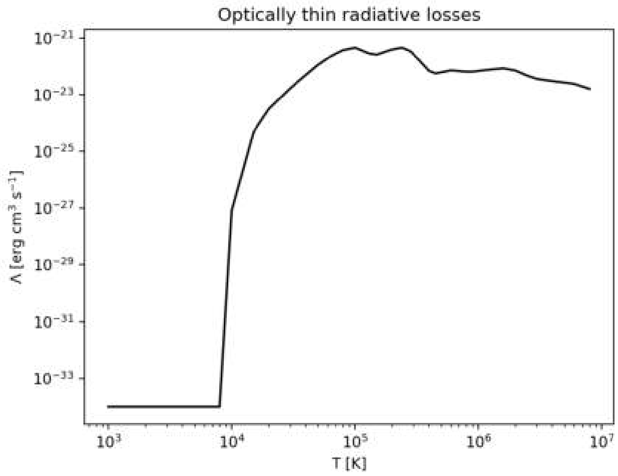

Figure 9. Function of optically thin radiative losses per unit emission measure, derived from the CHIANTI v. 7.0 database (E. Landi & F. Reale 2013), assuming coronal element abundances (K. Widing & U. Feldman 1992).

where $\Lambda(T)$ is the plasma emissivity per unit emission measure (integrated over all wavelengths), and $n_{\rm H}$ and $n_{\rm e}$ are the hydrogen and electron number density, respectively (assumed equal). The PLUTO code includes optically thin radiative losses in a fractional step formalism, which preserves the second-order time accuracy, since the advection and source steps are at least second-order accurate; the radiative loss values ($\Lambda(T)$) are computed at the temperature of interest using a table lookup/interpolation method. In particular, we considered the radiative losses from optically thin plasma per unit emission measure (shown in the plot of Figure 9), derived from the CHIANTI v. 7.0 database (e.g., E. Landi & F. Reale 2013), assuming coronal element abundances (K. Widing & U. Feldman 1992).

ORCID iDs

G. Cozzo https://orcid.org/0009-0005-4545-1010
Paola Testa https://orcid.org/0000-0002-0405-0668
J. Martinez-Sykora https://orcid.org/0000-0002-0333-5717
F. Reale https://orcid.org/0000-0002-1820-4824
P. Pagano https://orcid.org/0000-0001-5274-515X
F. Rappazzo https://orcid.org/0000-0001-9030-0418
V. Hansteen https://orcid.org/0000-0003-0975-6659
B. De Pontieu https://orcid.org/0000-0002-8370-952X
A. Petralia https://orcid.org/0000-0002-9882-1020
E. Alaimo https://orcid.org/0000-0002-9346-1732
F. Fiorentino https://orcid.org/0009-0000-6975-5127
F. D'Anca https://orcid.org/0000-0001-7834-5760
L. Sciortino https://orcid.org/0000-0002-4725-357X
M. Todaro https://orcid.org/0000-0002-3843-1637
U. Lo Cicero https://orcid.org/0000-0003-0318-3546
M. Barbera https://orcid.org/0000-0002-3188-7420

References

Alfvén, H. 1947, MNRAS, 107, 211
Anders, E., & Grevesse, N. 1989, GeCoA, 53, 197
Antolin, P., Pagano, P., Testa, P., Petralia, A., & Reale, F. 2021, NatAs, 5, 54
Arber, T., Longbottom, A., Gerrard, C., & Milne, A. 2001, JCoPh, 171, 151
Balsara, D. S., & Spicer, D. S. 1999, JCoPh, 149, 270
Baty, H., & Heyvaerts, J. 1996, A&A, 308, 935
Beveridge, C., Longcope, D., & Priest, E. R. 2003, SoPh, 216, 27
Boerner, P., Edwards, C., Lemen, J., et al. 2012, in The Solar Dynamics Observatory, ed. P. Chamberlin, W. D. Pesnell, & B. Thompson (Springer), 41
Bonet, J. A., Mrquez, I., Snchez Almeida, J., Cabello, I., & Domingo, V. 2008, ApJL, 687, L131
Bradshaw, S. J., & Cargill, P. J. 2013, ApJ, 770, 12
Breu, C., Peter, H., Cameron, R., et al. 2022, A&A, 658, A45
Browning, P., & Priest, E. 1986, A&A, 159, 129
Cargill, P. J., & Klimchuk, J. A. 2004, ApJ, 605, 911
Cho, K., Testa, P., De Pontieu, B., & Polito, V. 2023, ApJ, 945, 143
Cozzo, G., Pagano, P., Petralia, A., & Reale, F. 2023, Symm, 15, 627
Cozzo, G., Pagano, P., Reale, F., et al. 2025, A&A, 695, A40
Cozzo, G., Reid, J., Pagano, P., Reale, F., & Hood, A. W. 2023, A&A, 678, A40
Cozzo, G., Reid, J., Pagano, P., et al. 2024, A&A, 689, A184
Crosby, N. B., Aschwanden, M. J., & Dennis, B. R. 1993, SoPh, 143, 275
Dahlburg, R., Einaudi, G., Taylor, B., et al. 2016, ApJ, 817, 47
De Pontieu, B., Martínez-Sykora, J., Testa, P., et al. 2019, ApJ, 888, 3
De Pontieu, B., Testa, P., Martínez-Sykora, J., et al. 2022, ApJ, 926, 52
Del Zanna, G. 2013, A&A, 558, A73
Del Zanna, G., Dere, K., Young, P., & Landi, E. 2021, ApJ, 909, 38
Dennis, B. R. 1985, SoPh, 100, 465
Drake, J. F. 1971, SoPh, 16, 152
Edlén, B. 1943, ZA, 22, 30
Feldman, U. 1992, PhyS, 46, 202
Foster, A. R., & Testa, P. 2011, ApJL, 740, L52
Galsgaard, K., & Nordlund, Å. 1996, JGR, 101, 13 445
Gold, T., & Hoyle, F. 1960, MNRAS, 120, 89
Golub, L., Deluca, E., Austin, G., et al. 2007, SoPh, 243, 63
Grotrian, W. 1939, NW, 27, 555
Guarrasi, M., Reale, F., Orlando, S., Mignone, A., & Klimchuk, J. 2014, A&A, 564, A48
Guarrasi, M., Reale, F., & Peres, G. 2010, ApJ, 719, 576
Gudiksen, B. V., & Nordlund, Å. 2005, ApJ, 618, 1020
Hendrix, D., & Van Hoven, G. 1996, ApJ, 467, 887
Hermans, J., & Keppens, R. 2021, A&A, 655, A36
Hesse, M., & Schindler, K. 1988, JGRA, 93, 5559
Hood, A., Browning, P., & Van der Linden, R. 2009, A&A, 506, 913
Hood, A., & Priest, E. 1979, A&A, 77, 233
Hood, A. W., Cargill, P., Browning, P., & Tam, K. 2016, ApJ, 817, 5
Howson, T. A., & De Moortel, I. 2022, A&A, 661, A144
Hudson, H. 2010, Heliophysics: Space Storms and Radiation: Causes and Effects (Cambridge Univ. Press), 123
Johnston, C., & Bradshaw, S. 2019, ApJL, 873, L22
Johnston, C. D., Cargill, P., Hood, A., et al. 2020, A&A, 635, A168
Johnston, C. D., Daldorff, L. K., Klimchuk, J. A., et al. 2025, ApJ, 994, 139
Johnston, C. D., Hood, A. W., De Moortel, I., Pagano, P., & Howson, T. A. 2021, A&A, 654, A2
Kliem, B., Török, T., Titov, V. S., et al. 2014, ApJ, 792, 107
Klimchuk, J., Patsourakos, S., & Cargill, P. 2008, ApJ, 682, 1351
Klimchuk, J. A. 2015, RSPTA, 373, 20140256
Kondrashov, D., Feynman, J., Liewer, P., & Ruzmaikin, A. 1999, ApJ, 519, 884
Landi, E., & Reale, F. 2013, ApJ, 772, 71
Landini, M., & Monsignori Fossi, B. 1975, A&A, 42, 213
Lemen, J. R., Title, A. M., Akin, D. J., et al. 2012, SoPh, 275, 17
Linton, M., Dahlburg, R., & Antiochos, S. 2001, ApJ, 553, 905
Liu, R. 2020, RAA, 20, 165
Melrose, D. 1997, ApJ, 486, 521
Mignone, A., Bodo, G., Massaglia, S., et al. 2007, ApJS, 170, 228
Ng, C., Lin, L., & Bhattacharjee, A. 2012, ApJ, 747, 109
Parker, E. N. 1988, ApJ, 330, 474
Parnell, C. E., & De Moortel, I. 2012, RSPTA, 370, 3217
Peter, H., & Dwivedi, B. N. 2014, FrASS, 1, 2
Poduval, B., DeForest, C., Schmelz, J., & Pathak, S. 2013, ApJ, 765, 144
Pontin, D., Wilmot-Smith, A., Hornig, G., & Galsgaard, K. 2011, A&A, 525, A57
Rappazzo, A., Velli, M., & Einaudi, G. 2013, ApJ, 771, 76
Rappazzo, A., Velli, M., Einaudi, G., & Dahlburg, R. 2008, ApJ, 677, 1348
Rappazzo, A. F., Velli, M., Einaudi, G., & Dahlburg, R. 2007, ApJL, 657, L47
Reale, F. 2007, A&A, 471, 271
Reale, F. 2014, LRSP, 11, 1

Reale, F., Guarrasi, M., Testa, P., et al. 2011, ApJL, 736, L16
Reale, F., Orlando, S., Guarrasi, M., et al. 2016, ApJ, 830, 21
Reid, J., Cargill, P., Hood, A. W., Parnell, C. E., & Arber, T. D. 2020, A&A, 633, A158
Reid, J., Hood, A. W., Parnell, C. E., Browning, P., & Cargill, P. 2018, A&A, 615, A84
Rempel, M. 2016, ApJ, 834, 10
Roe, P. L. 1986, AnRFM, 18, 337
Rosner, R., Tucker, W. H., & Vaiana, G. 1978, ApJ, 220, 643
Schindler, K., Hesse, M., & Birn, J. 1988, JGR, 93, 5547
Sen, S., & Moreno-Insertis, F. 2025, A&A, 699, A106
Spitzer, L., Jr, & Härm, R. 1953, PhRv, 89, 977
Sweby, P. K. 1985, Large-scale Computations in Fluid Mechanics
Tam, K. V., Hood, A. W., Browning, P., & Cargill, P. 2015, A&A, 580, A122
Taylor, J. B. 1974, PhRvL, 33, 1139
Testa, P., De Pontieu, B., Allred, J., et al. 2014, Sci, 346, 1255724
Testa, P., De Pontieu, B., Martínez-Sykora, J., et al. 2013, ApJL, 770, L1
Testa, P., Drake, J. J., & Landi, E. 2012, ApJ, 745, 111
Testa, P., Polito, V., & De Pontieu, B. 2020, ApJ, 889, 124
Testa, P., & Reale, F. 2012, ApJL, 750, L10
Testa, P., & Reale, F. 2020, ApJ, 902, 31
Testa, P., & Reale, F. 2023, in Handbook of X-ray and Gamma-ray Astrophysics, ed. C. Bambi & A. Santangelo (Springer), 1
Testa, P., Saar, S. H., & Drake, J. J. 2015, RSPTA, 373, 20140259
Vaiana, G., Krieger, A., & Timothy, A. 1973, SoPh, 32, 81
Vekstein, G. 2009, A&A, 499, L5
Vögler, A., Shelyag, S., Schüssler, M., et al. 2005, A&A, 429, 335
Widing, K., & Feldman, U. 1992, ApJ, 392, 715
Wilmot-Smith, A. 2015, RSPTA, 373, 20140265